Monthly Notices
of the
ROYAL ASTRONOMICAL SOCIETY

MNRAS **516,** 1741–1751 (2022)
Advance Access publication 2022 August 22

https://doi.org/10.1093/mnras/stac2329

H I properties of satellite galaxies around local volume hosts

Ananthan Karunakaran ,[1★] Kristine Spekkens ,[2,3] Rhys Carroll,[2] David J. Sand ,[4] Paul Bennet ,[5]
Denija Crnojević ,[6] Michael G. Jones [4] and Burçın Mutlu-Pakdıl [7,8,9]

[1] *Instituto de Astrofísica de Andalucía (CSIC), Glorieta de la Astronomía, E-18008 Granada, Spain*
[2] *Department of Physics and Space Science, Royal Military College of Canada, P.O. Box 17000, Station Forces Kingston, ON K7K 7B4, Canada*
[3] *Department of Physics, Engineering Physics and Astronomy, Queen's University, Kingston, ON K7L 3N6, Canada*
[4] *Steward Observatory, University of Arizona, 933 North Cherry Avenue, Rm. N204, Tucson, AZ 85721-0065, USA*
[5] *Space Telescope Science Institute, 3700 San Martin Drive, Baltimore, MD 21218, USA*
[6] *University of Tampa, 401 West Kennedy Boulevard, Tampa, FL 33606, USA*
[7] *Kavli Institute for Cosmological Physics, University of Chicago, Chicago, IL 60637, USA*
[8] *Department of Astronomy and Astrophysics, University of Chicago, Chicago, IL 60637, USA*
[9] *Department of Physics and Astronomy, Dartmouth College, 6127 Wilder Laboratory, Hanover, NH 03755, USA*

Accepted 2022 August 15. Received 2022 August 15; in original form 2022 June 23

ABSTRACT

We present neutral atomic hydrogen (H I) observations using the Robert C. Byrd Green Bank Telescope along the lines of sight to 49 confirmed or possible dwarf satellite galaxies around eight Local Volume systems (M104, M51, NGC 1023, NGC 1156, NGC 2903, NGC 4258, NGC 4565, and NGC 4631). We detect the H I reservoirs of two candidates (dw0934+2204 and dw1238−1122) and find them to be background sources relative to their nearest foreground host systems. The remaining 47 satellite candidates are not detected in H I, and we place stringent 5σ upper limits on their H I mass. We note that some (15/47) of our non-detections stem from satellites being occluded by their putative host's H I emission. In addition to these new observations, we compile literature estimates on the H I mass for an additional 17 satellites. We compare the H I properties of these satellites to those within the Local Group, finding broad agreement between them. Crucially, these observations probe a 'transition' region between $-10 \gtrsim M_V \gtrsim -14$ where we see a mixture of gas-rich and gas-poor satellites. While there are many gas-poor satellites within this region, some are gas-rich and this suggests that the transition towards predominantly gas-rich satellites occurs at $L_V \sim 10^7 L_\odot$, in line with simulations. The observations presented here are a key step toward characterizing the properties of dwarf satellite galaxies around Local Volume systems and future wide-field radio surveys with higher angular resolution (e.g. WALLABY) will vastly improve upon the study of such systems.

Key words: galaxies: dwarf – galaxies: evolution – Local Group – radio lines: galaxies.

1 INTRODUCTION

Satellite galaxies provide a unique insight into the hierarchical galaxy formation and evolution process within the Lambda cold dark matter framework. Due to their proximity, the vast majority of detailed studies at low luminosities have been conducted with satellite dwarf galaxies in the Local Group. Several interesting trends have been discovered, some of which appear to be in tension with the current cosmological framework (e.g. Bullock & Boylan-Kolchin 2017), while others probe the environmental effects of the Milky Way and M31 on their satellites. Environmental trends in satellite dwarf galaxy properties are now well-established within the Local Group: low-mass ($M_* \lesssim 10^6\,\mathrm{M}_\odot$) dwarf satellites within the virial radius of the Milky Way or M31 are generally quenched and gas poor, while those with higher masses ($M_* \gtrsim 10^8\,\mathrm{M}_\odot$) or beyond the virial radius are generally star-forming and gas-rich (Grcevich & Putman 2009; Spekkens et al. 2014; Putman et al. 2021). Similarly, gas-rich and star-forming dwarf galaxies are ubiquitous in lower density environments (i.e. the field Geha et al. 2012; Huang et al. 2012). Exceptions to these trends include quenched 'backsplash' dwarf galaxies identified beyond the virial radius (Teyssier, Johnston & Kuhlen 2012), or ultrafaint dwarf galaxies plausibly quenched by reionization that appear in the field (e.g. Sand et al. 2022).

Within the last decade, great strides have been made in constraining the quenching mechanisms of satellite galaxies from a theoretical perspective. The aforementioned environmental trends are also present in simulations of Milky Way-like ($M_{\mathrm{vir}} \sim 10^{12}\,\mathrm{M}_\odot$) and Local Group-like systems (Fillingham et al. 2015; Fattahi et al. 2016; Wetzel et al. 2016; Simpson et al. 2018; Garrison-Kimmel et al. 2019; Akins et al. 2021; Karunakaran et al. 2021; Font et al. 2022), regardless of their implementation (i.e. subgrid) of underlying astrophysical processes. Pushing these comparisons to lower masses with larger satellite samples is an important test for galaxy formation simulations since lower mass systems are more susceptible to these details of these processes due to their weaker gravitational potentials.

These advances on the theoretical front are complemented by expanding studies of satellite dwarf galaxies beyond the Local Group that build upon the seminal works of Zaritsky et al. (1993, 1997).

★ E-mail: karunakarananthan@gmail.com

Published by Oxford University Press on behalf of Royal Astronomical Society

These studies, whether via integrated light (Merritt, van Dokkum & Abraham (Merritt, van Dokkum & Abraham 2014; Karachentsev et al. 2015; Javanmardi et al. 2016; Bennet et al. 2017; Geha et al. 2017; Müller et al. 2017; Smercina et al. 2018; Carlsten et al. 2019, 2022a; Mao et al. 2021) or via resolved stars (Chiboucas, Karachentsev & Tully 2009; Chiboucas et al. 2013; Carlin et al. 2016; Crnojević et al. 2016, 2019; Bennet et al. 2019, 2020; Mutlu-Pakdil et al. 2021, 2022), have discovered dozens of new satellites in nearby systems. These growing samples enable increasingly detailed comparisons to the Local Group satellite system.

Carlsten et al. (2020) present a sample of 155 satellite candidates around 10 Local Volume (<12 Mpc) hosts detected in CFHT imaging. They then subsequently employed the surface brightness fluctuation (SBF) method to estimate distances to these candidates (Carlsten et al. 2021), confirming 55 new satellites. While this Local Volume sample is near 100 per cent complete down to $M_V \gtrsim -9$ and $\mu_{0,V} \lesssim 26.5$mag arcsec^{-2}, its spatial coverage within the virial radius of the hosts is much lower compared to other surveys of Milky Way-like systems (Geha et al. 2017; Mao et al. 2021). We note, however, that this issue of spatial coverage is remedied by the Exploration of Local VolumE Satellites (ELVES, Carlsten et al. 2022a) survey which supersedes and is significantly more spatially complete within the hosts' virial radii relative to the Carlsten et al. (2020) sample. Nevertheless, the increased photometric completeness enables studies of the environmental effect on low-mass satellites by their hosts for the first time.

The neutral atomic hydrogen (H I) content is a crucial complementary component to these wide-field optical satellite searches. Obtaining measurements of the satellite H I content beyond the Local Group will place observational constraints on the environmental effects on these low-mass systems and also constrain the host-to-host scatter. As H I is the initial fuel for star formation, its presence or lack thereof in satellites enables a better understanding of their past and future evolution. While the SBF distance method allows for a relatively robust estimate, there are occasions where it does not perform well (e.g. for irregular morphologies, Karunakaran et al. 2020a; Carlsten et al. 2021), and spectroscopic observations can help in these edge cases.

Although, by-and-large, massive satellites are gas-rich and low-mass satellites are gas-poor within the Local Group, the threshold within this broad mass range at which the gas richness of the population transitions from low to high is only just beginning to be probed systematically (i.e. Carlsten et al. 2020, 2022a). This 'transition' region lies above the stellar masses of the bulk of the Local Group satellites, but below the stellar masses of the bulk of the satellites of Milky Way-like systems that have in so far been detected in the Local Volume (Geha et al. 2017; Mao et al. 2021). H I observations of satellite candidates in this transition region, therefore, bridge the data gap between the Local Group and Local Volume while also constraining the mass dependence of the underlying quenching mechanisms at work.

In this paper, we present new H I observations of 49 dwarf satellite candidates around eight Local Volume hosts from the Carlsten et al. (2020) sample with the Robert C. Byrd Green Bank Telescope[1] (GBT) and additionally compile 17 H I measurements from the literature. With this study, we constrain the H I gas content and gas richness of systems that reside in this aforementioned transition region for the first time. In addition, we lay the foundation for more comprehensive studies of the H I properties of satellites around massive hosts in the Local Volume and beyond, while also highlighting some potentially interesting trends that will be solidified with future expanded studies.

The structure of this paper is as follows. In Section 2 and 3, we describe our sample selection and our H I observations. We present our derived and compiled H I results in Section 4, along with a brief discussion of the properties of their optical counterparts and a comparison to the Local Group satellites. In Section 5, we briefly discuss this work in a broader context and provide our summary.

2 SAMPLE SELECTION

We select our H I follow-up sample from the Local Volume survey conducted by Carlsten et al. (2020, hereafter C20) and Carlsten et al. (2021, hereafter C21). A total of 155 satellite candidates around 10 Local Volume hosts were presented in C20 with subsequent SBF distance estimates presented in C21. The distance estimates were used to classify satellite candidates as 'confirmed', 'possible' (unconstrained), or 'background' with respect to their putative hosts. A total of 55 of the C20 candidates were confirmed as satellites, 48 classified as possible, and the remaining 49 classified as background systems. Based on the mock dwarf injection/recovery testing presented in C21, the sample is considered to be near 100 per cent complete for $M_V \gtrsim -9$, $\mu_{0,V} \lesssim 26.5$ mag arcsec^{-2}, and $r_{\rm eff} > 4$ arcsec. However, we note that the spatial coverage of the C20 sample is not as complete. Only six of the nine hosts studied here have greater than 70 per cent coverage within a 150 kpc projected radius. We keep this caveat in mind for our interpretation.

For our H I follow-up sample, we select all satellites brighter than $M_V = -9.5$ ($M_* \sim 10^6\,{\rm M}_\odot$) that are classified as 'confirmed' or 'possible'. We opted for this selection limit primarily to minimize the amount of observing time that would be required, however, it also ensures that we are well within the photometric completeness limit of the sample. This selection criterion produces a sample of 66 satellite candidates (48 confirmed, 18 possible), 17 of which have H I measurements (either detections or upper limits) in the literature. We list the basic properties of the studied sample in Table 1. Throughout this work, we assume that the distances to the satellites are the same as their hosts unless otherwise stated.

3 OBSERVATIONS AND DATA REDUCTION

We performed a total of ∼72 h of observations (projects GBT20A-576 and GBT21A-388, PI:Karunakaran) with the GBT using the *L*-band receiver and the VErsatile GBT Astronomical Spectrometer (VEGAS) along the lines of sight to 49 satellite candidates from C20 and C21 without literature H I detections (see Table 1). GBT20A-576 focused on the brighter ($M_V \leq -11$ mag) subset of confirmed or possible satellite candidates, while GBT21-388 focused on the fainter ($-9.5 \geq M_V > -11$) targets. Our observing strategy for each subset differed. For the brighter subset, we used VEGAS in Mode 10 which provides a relatively narrow bandwidth (23.44 MHz, $\sim 5000\,{\rm km\,s^{-1}}$). Given the robustness of the SBF technique at higher luminosity, a wider bandpass would not have benefited the search for the H I reservoirs of these systems and would likely have been more detrimental in terms of radio frequency interference (RFI). Conversely, for the fainter subset, we used VEGAS in Mode 7 which provides a wider bandpass (100 MHz, $\sim 21\,000\,{\rm km\,s^{-1}}$). This wider bandwidth affords the ability to search for potential H I signals along the LOS out to velocities of $14\,000\,{\rm km\,s^{-1}}$ (~ 200 Mpc). While we could have centred our bandpass to probe a greater velocity range, we have found, from previous observations, that there is strong,

---

[1] The Green Bank Observatory is a facility of the National Science Foundation operated under cooperative agreement by Associated Universities, Inc.

Table 1. Properties of confirmed and possible satellites from the Local Volume sample. Column (1): dwarf satellite names. Columns (2) and (3): J2000 RA and Dec. Columns (4) and (5): putative host galaxy and host distance. Column (6): *V*-band absolute magnitude taken from C21. Column (7): association, either confirmed or possible based on C21. Column (8): H I source abbreviations are as follows: V77 = van Albada (1977), S84 = Sancisi et al. (1984), B03 = Braun, Thilker & Walterbos (2003), D05 = Dahlem et al. (2005), I09 = Irwin et al. (2009), W13 = Wolfinger et al. (2013), C15 = Courtois & Tully (2015), H18 = Haynes et al. (2018), K20 = Karunakaran et al. (2020b), K22 = this work. Column (9): H I detection or non-detection. Columns: (10) and (11): Integrated flux and RMS noise at a velocity resolution of 50 $\mathrm{km\,s^{-1}}$. Column (12): observing time with the GBT. Columns (13) and (14): logarithm of H I mass and H I mass to *V*-band luminosity ratio. In the case of non-detections, 5σ upper limits are reported.

Name (1)	α (H:M:S) (2)	δ (D:M:S) (3)	Host (4)	$D_{\rm Host}$ (Mpc) (5)	M_V (mag) (6)	C21 Assoc. (7)	H I Source (8)	H I Det? (9)	Int. flux ($\mathrm{Jy\,km\,s^{-1}}$) (10)	σ_{50} (mJy) (11)	Time (h) (12)	log($\frac{M_{\rm HI}}{M_\odot}$) (13)	$\frac{M_{\rm HI}}{L_V}$ ($\frac{M_\odot}{L_\odot}$) (14)
dw0233+3852	02:33:42.70	38:52:20.10	NGC 1023	10.4	– 11.92	C	K22		–	0.87	0.3	<6.74	<1.13
dw0235+3850[b]	02:35:54.20	38:50:10.30	NGC 1023	10.4	– 13.52	C	K22		–	0.92	0.3	<6.77	<0.27
IC239	02:36:28.10	38:58:08.50	NGC 1023	10.4	– 19.1	C	B03	Y	140.9	–	–	9.56	0.99
dw0237+3855[b]	02:37:18.60	38:55:59.20	NGC 1023	10.4	– 15.19	C	K22		–	0.94	0.3	<6.78	<0.06
dw0237+3836	02:37:39.40	38:36:01.20	NGC 1023	10.4	– 12.12	C	K22		–	0.84	0.3	<6.73	<0.90
dw0238+3805	02:38:41.00	38:05:06.50	NGC 1023	10.4	– 13.6	P	K22		–	0.98	0.3	<6.79	<0.27
dw0239+3926	02:39:19.90	39:26:02.10	NGC 1023	10.4	– 12.42	C	K22		–	0.7	0.3	<6.65	<0.58
dw0239+3902[b]	02:39:47.00	39:02:50.40	NGC 1023	10.4	– 9.79	C	K22		–	0.7	1.5	<6.65	<6.54
UGC2157	02:40:25.00	38:33:46.90	NGC 1023	10.4	– 16.4	C	C15	Y	1.44	–	–	7.40	0.1
dw0240+3854	02:40:33.00	38:54:01.40	NGC 1023	10.4	– 13.49	C	S84	Y	0.8	–	–	7.31	0.98
dw0240+3903	02:40:37.10	39:03:33.60	NGC 1023	10.4	– 15.1	C	S84	Y	3.7	–	–	7.97	1.03
dw0240+3922	02:40:39.60	39:22:45.10	NGC 1023	10.4	– 13.51	C	S84	Y	1.3	–	–	7.52	1.57
dw0241+3904[b]	02:41:00.40	39:04:20.60	NGC 1023	10.4	– 14.34	C	K22		–	0.87	0.3	<6.74	<0.12
UGC2165	02:41:15.50	38:44:38.90	NGC 1023	10.4	– 16.23	C	K22		–	0.91	0.3	<6.76	<0.02
dw0241+3829	02:41:54.20	38:29:53.60	NGC 1023	10.4	– 10.85	P	K22		–	4.81	1.9	<7.49	<16.85
dw0243+3915	02:43:55.00	39:15:20.70	NGC 1023	10.4	– 11.43	P	K22		–	0.73	0.5	<6.66	<1.49
dw0300+2514[b]	03:00:17.80	25:14:56.00	NGC 1156	7.6	– 10.66	P	K22		–	1.05	0.5	<6.55	<2.34
dw0301+2446	03:01:32.20	24:46:59.40	NGC 1156	7.6	– 10.76	P	K22		–	2.31	0.3	<6.89	<4.68
dw0930+2143	09:30:40.00	21:43:27.10	NGC 2903	8	– 11.01	C	I09	Y	0.14	–	–	<6.32	1.00
UGC5086	09:32:48.80	21:27:56.20	NGC 2903	8	– 14.13	C	I09		–	–	–	<5.66	<0.01
dw0934+2204[a]	09:34:22.00	22:04:53.90	NGC 2903	8	– 14.96	P	K22	Y	0.18	0.34	1.6	8.29	2.48
NGC 4248[b]	12:17:50.20	47:24:33.40	NGC 4258	7.2	– 16.86	C	V77	Y	4.19	–	–	7.71	0.11
LVJ1218+4655	12:18:11.20	46:55:02.00	NGC 4258	7.2	– 12.93	C	W13	Y	6.26	–	–	7.88	6.19
dw1219+4743	12:19:06.20	47:43:49.30	NGC 4258	7.2	– 11.00	C	K22		–	0.78	0.2	<6.38	<1.14
UGC7356[b]	12:19:09.00	47:05:23.90	NGC 4258	7.2	– 14.32	C	K22		–	1.36	0.2	<6.62	<0.09
dw1220+4922	12:20:14.40	49:22:51.60	NGC 4258	7.2	– 9.59	P	K22		–	0.26	2.9	<5.91	<1.41
dw1220+4649	12:20:54.90	46:49:48.40	NGC 4258	7.2	– 10.76	C	K22		–	0.78	0.5	<6.37	<1.41
dw1223+4739	12:23:46.20	47:39:32.70	NGC 4258	7.2	– 11.54	C	K22		–	0.88	0.2	<6.43	<0.78
dw1233+2535	12:33:11.00	25:35:55.20	NGC 4565	11.9	– 11.97	P	K22		–	0.84	0.2	<6.84	<1.37
dw1233+2543	12:33:18.40	25:43:35.10	NGC 4565	11.9	– 10.01	P	K22		–	0.19	3.8	<6.21	<1.92
dw1234+2531	12:34:24.20	25:31:20.20	NGC 4565	11.9	– 14.03	C	K22		–	0.54	0.5	<6.65	<0.13
dw1234+2618	12:34:57.60	26:18:50.80	NGC 4565	11.9	– 10.32	P	K22		–	0.53	3.5	<6.65	<3.96
dw1235+2616	12:35:22.30	26:16:14.20	NGC 4565	11.9	– 10.15	P	K22		–	0.38	3.7	<6.50	<3.32
NGC 4562	12:35:34.70	25:51:01.30	NGC 4565	11.9	– 17.15	C	H18	Y	6.22	–	–	8.32	0.34
IC3571	12:36:20.00	26:05:03.50	NGC 4565	11.9	– 13.90	C	D05	Y	0.91	–	–	7.48	1.01
dw1236+2634	12:36:58.60	26:34:42.80	NGC 4565	11.9	– 9.50	P	K22		–	0.3	4.0	<6.40	<4.84
dw1237+2602[b]	12:37:01.20	26:02:09.60	NGC 4565	11.9	– 12.64	C	K22		–	0.91	0.2	<6.88	<0.80
dw1237+2605	12:37:26.80	26:05:08.70	NGC 4565	11.9	– 10.85	P	K22		–	0.37	1.8	<6.49	<1.71
dw1237+2637	12:37:42.80	26:37:27.60	NGC 4565	11.9	– 10.46	P	K22		–	0.23	3.6	<6.29	<1.54
dw1239+3230	12:39:05.00	32:30:16.50	NGC 4631	7.4	– 10.31	C	K20	Y	0.19	–	–	6.39	2.22
dw1239+3251	12:39:19.60	32:51:39.30	NGC 4631	7.4	– 9.65	C	K22		–	0.22	2.6	<5.85	<1.19
dw1240+3216[b]	12:40:53.00	32:16:55.90	NGC 4631	7.4	– 10.64	C	K22		–	0.56	0.6	<6.26	<1.20
dw1240+3247	12:40:58.50	32:47:25.00	NGC 4631	7.4	– 13.61	C	K22		–	0.86	0.2	<6.44	<0.12
dw1241+3251	12:41:47.10	32:51:27.30	NGC 4631	7.4	– 13.74	C	H18	Y	1.98	–	–	7.41	0.98
NGC 4627	12:41:59.70	32:34:26.20	NGC 4631	7.4	– 16.7	C	W13		–	–	–	<9.76	<14.57
dw1242+3237[b]	12:42:06.20	32:37:18.70	NGC 4631	7.4	– 10.71	C	K22		–	0.64	0.5	<6.32	<1.30
dw1242+3158[b]	12:42:31.40	31:58:09.20	NGC 4631	7.4	– 10.51	C	K22		–	0.58	0.8	<6.27	<1.40
dw1243+3228[b]	12:43:24.80	32:28:55.30	NGC 4631	7.4	– 12.88	C	K22		–	0.83	0.2	<6.43	<0.23
NGC 4656	12:43:57.70	32:10:05.30	NGC 4631	7.4	– 18.9	C	H18	Y	250.18	–	–	9.51	1.07
dw1237−1125	12:37:11.60	−11:25:59.30	M104	9.55	– 12.02	C	K22		–	0.59	0.4	<6.50	<0.60
dw1238−1122[a]	12:38:33.70	−11:22:05.10	M104	9.55	– 12.6	P	K22	Y	0.57	0.71	0.4	8.17	1.36
dw1239−1159	12:39:09.10	−11:59:12.20	M104	9.55	– 11.21	C	K22		–	0.6	0.8	<6.51	<1.28
dw1239−1143	12:39:15.30	−11:43:08.10	M104	9.55	– 13.70	C	K22		–	0.74	0.4	<6.60	<0.16
dw1239−1113	12:39:32.70	−11:13:36.00	M104	9.55	– 12.23	C	K22		–	0.66	0.4	<6.55	<0.54
dw1239−1120	12:39:51.50	−11:20:28.70	M104	9.55	– 10.73	C	K22		–	0.56	0.6	<6.48	<1.84
dw1239−1144	12:39:54.90	−11:44:45.50	M104	9.55	– 12.85	C	K22		–	0.74	0.4	<6.60	<0.35
dw1240−1118	12:40:09.40	−11:18:49.80	M104	9.55	– 14.32	C	K22		–	0.52	0.4	<6.44	<0.06
dw1240−1140[b]	12:40:17.60	−11:40:45.70	M104	9.55	– 11.01	C	K22		–	0.87	0.5	<6.67	<2.22
dw1241−1131	12:41:02.80	−11:31:43.70	M104	9.55	– 10.44	C	K22		–	0.33	1.9	<6.24	<1.41
dw1241−1153	12:41:12.10	−11:53:29.70	M104	9.55	– 11.82	C	K22		–	0.87	0.3	<6.67	<1.04
dw1241−1155	12:41:18.70	−11:55:30.80	M104	9.55	– 12.72	C	K22		–	0.7	0.4	<6.57	<0.37
dw1242−1116	12:42:43.80	−11:16:26.00	M104	9.55	– 12.05	P	K22		–	0.77	0.4	<6.61	<0.75
dw1328+4703[b]	13:28:24.70	47:03:54.80	M51	8.6	– 9.62	P	K22		–	0.27	2.6	<6.07	<1.99
NGC 5195	13:29:59.60	47:15:58.10	M51	8.6	– 20.2	C	C15	Y	101.56	–	–	9.25	0.18
dw1330+4731[b]	13:30:33.90	47:31:33.10	M51	8.6	– 9.89	P	K22		–	0.28	2.6	<6.08	<1.61
NGC 5229	13:34:03.00	47:54:49.80	M51	8.6	– 16.2	C	C15	Y	22.23	–	–	8.59	1.54

[a] Detections from this work. [b] contaminating H I emission from their host or neighbour.

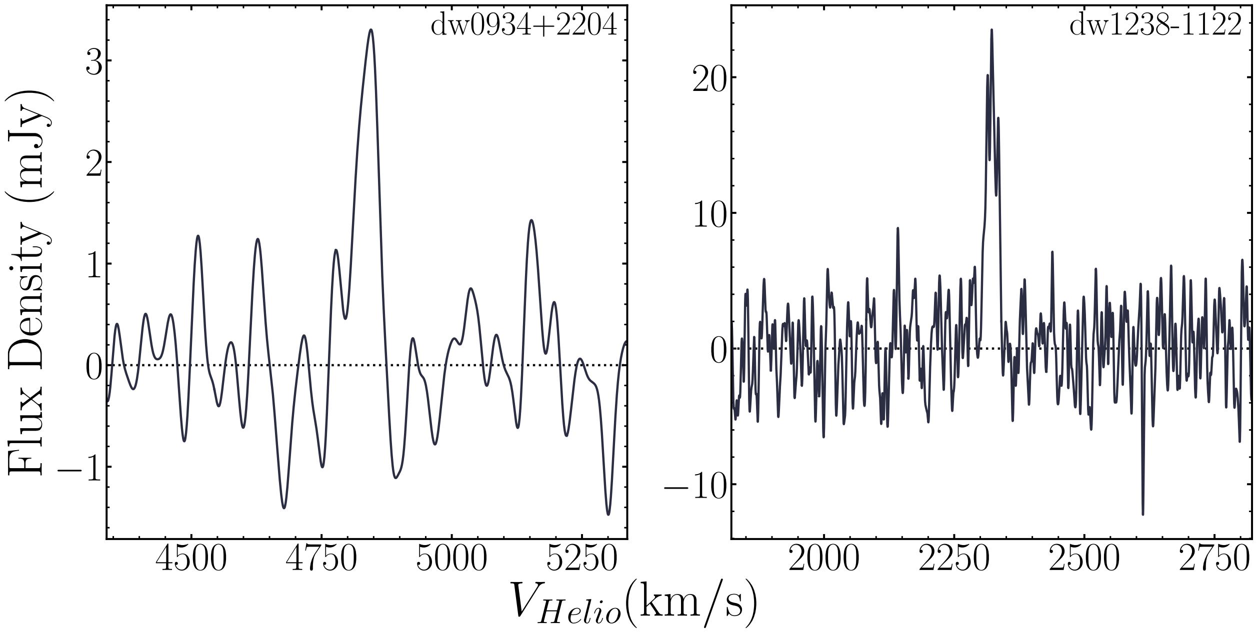

Figure 1. H I spectra for dw0934+2204 and dw1238−1122 from our GBT observations at the resolution, ΔV, listed alongside their derived H I properties in Table 2. The horizontal dotted line shows a flux density of 0 mJy. These detections confirm that the satellite candidates are in fact in the background of their putative hosts, and are therefore field dwarfs.

intermittent RFI at higher (lower) velocities (frequencies) that can severely affect these deep observations. To estimate the required sensitivities (i.e. RMS noise levels) to detect the H I reservoirs of these sources, we used their V-band luminosities with an assumed gas-richness of $M_{\rm H\,I}/L_V = 1{\rm M}_\odot/L_\odot$ across 25 km s^{-1} channels. This gas-richness limit generally separates gas-poor satellites and gas-rich field dwarf galaxies within the Local Group (Spekkens et al. 2014) and is also $\sim 2\sigma$ below the scaling relations of Bradford, Geha & Blanton (2015).

We follow the standard procedure to calibrate the raw GBT spectra using GETPS in GBTIDL[2] as presented in Karunakaran et al. (2020a, 2020b). As part of this procedure, we flag and replace narrow-band RFI with local noise values in a given 5-s integration (a data dump) and remove entire data dumps that are affected by broad-band RFI, specifically the 1.38-GHz GPS-L3 signal (see Karunakaran et al. 2020a for more details). Following these standard RFI excision measures, we found that several of the calibrated spectra were affected by unforeseen and infrequent RFI that resulted in broad-band artefact. Therefore, we opted to remove these affected data dumps ($\sim 15-30\%$ of them depending on the target) and repeat the calibration process. For these reasons, we were unable to reach the desired $M_{\rm H\,I}/L_V$ for several of our targets.

We visually search for potentially significant H I emission in the calibrated, RFI-excised spectra that we smooth to various velocity resolutions $5 < \Delta V < 50$ km s^{-1}. In Table 1, we list representative RMS noise values (σ_{50}) for all of our targets in the emission-free regions of each spectrum at a velocity resolution $\Delta V = 50$km s^{-1}. We note that, while this velocity width is large relative to the faint dwarfs of the Local Group, it is similar to the mean velocity widths of H I-detected dwarfs and falls near the middle of the broad range of expected dwarf velocity widths (Huang et al. 2012; Poulain et al. 2022). We detect H I along the LOS to two of our targets, dw0934+2204 and dw1238−1122. We show their H I spectra in Fig. 1 and list their derived properties in Table 2. For the remaining 47 targets, we estimate upper limits on $M_{\rm H\,I}$ and $M_{\rm H\,I}/L_V$, and list them in Table 1. We note that ∼30 per cent (15/47) of the non-detections have H I emission from their host's or a nearby neighbour's H I disc. While this leads to less stringent constraints on whether or not they are truly gas-rich satellites, we treat these systems as non-detections and discuss this issue in more detail in Section 4.2 and in the context of their optical properties in Section 4.4.1.

4 RESULTS

4.1 H I Detections

Prior to deriving their properties, we first confirm that we have correctly associated our two H I detections with their targeted optical counterparts and not nearby interlopers. Given the well-characterized response pattern of the GBT beam (FWHM ∼ 9 arcmin) at 1.420-GHz down to ≈−30dB (Spekkens et al. 2013), we can search for potential interlopers and confirm the association of these detections to the satellite candidates. We performed a search through NED[3] within a radius of 30 arcmin and within ±500km s^{-1} of the systemic velocity of the H I detection. We also visually searched through the Legacy Survey Viewer[4] and Pan-STARRS cutouts[5] for potential gas-rich sources (i.e. relatively blue, late-type or irregular galaxies) within 30 arcmin. We find no such sources in our search, strongly suggesting that the H I detections are the counterparts to the two satellite candidates in our sample.

---

[2] https://gbtidl.nrao.edu/index.shtml

[3] The NASA/IPAC Extragalactic Database (NED) is operated by the Jet Propulsion Laboratory, California Institute of Technology, under contract with the National Aeronautics and Space Administration.

[4] https://www.legacysurvey.org/viewer

[5] http://ps1images.stsci.edu/cgi-bin/ps1cutouts

Table 2. H I Properties of dwarf satellite candidates with H I detections. Columns (2) and (3): velocity resolution and RMS noise at Δ_V. Column (4): systemic velocity of the H I detection. Column (5): velocity width corrected for instrumental and redshift broadening. Column (6): integrated H I flux density. Column (7): distance calculated from $V_{\rm sys}$ in Column (4) using the Hubble–Lemaître law assuming $H_0 = 70\,{\rm km\,s^{-1}\,Mpc^{-1}}$. Columns (8) and (9): logarithm of the *V*-band luminosity and H I mass. Column (10): H I mass to *V*-band luminosity ratio.

Name (1)	ΔV (km s^{-1}) (2)	$\sigma_{\Delta V}$ (mJy) (3)	$V_{\rm sys}$ (km s^{-1}) (4)	$W_{50,\,c}$ (km s^{-1}) (5)	$S_{\rm H\,I}$ (Jy km s^{-1}) (6)	$D_{\rm H\,I}$ (Mpc) (7)	$\log(\frac{L_V}{L_\odot})$ (8)	$\log(\frac{M_{\rm H\,I}}{\rm M_\odot})$ (9)	$(\frac{M_{\rm H\,I}}{L_V})$ $(\frac{\rm M_\odot}{L_\odot})$ (10)
dw0934+2204	20	0.6	4837 ± 2	39 ± 3	0.18 ± 0.05	69 ± 5	7.90 ± 0.08	8.29 ± 0.13	2.48 ± 0.84
dw1238−1122	15	1.3	2322 ± 3	14 ± 4	0.57 ± 0.08	33 ± 5	8.04 ± 0.26	8.17 ± 0.11	1.36 ± 0.89

We follow the methods described in Karunakaran et al. (2020a) to derive the properties of our two H I detections. We first estimate the systemic velocities, $V_{\rm sys}$, and velocity widths, W_{50}, by performing a linear fit at each edge of the H I profile between 15 and 85 per cent of the peak H I flux. From these fits, we find the velocity that corresponds to 50 per cent of the peak flux at each edge and their average provides $V_{\rm sys}$, while their difference provides W_{50}. We correct W_{50} for instrumental broadening and cosmological redshift, resulting in a corrected velocity width $W_{50,\,\rm c}$. The adopted 50 per cent uncertainty on the instrumental broadening correction (see Springob et al. 2005) dominates the uncertainties of both $V_{\rm sys}$ and $W_{50,\,\rm c}$. These values and their uncertainties are listed in Table 2.

Before we estimate $M_{\rm H\,I}$ for our detections, we first must estimate their distances. We use our derived $V_{\rm sys}$ values together with the Hubble–Lemaître law assuming $H_0 = 70\,{\rm km\,s^{-1}\,Mpc^{-1}}$ to estimate their distances and we assume distance uncertainties of 5 Mpc to account for potentially large peculiar velocities (Leisman et al. 2017). Both of these sources are in the distant background of their putative host galaxies and within the Hubble flow. dw0934+2204 and dw1238−1122 are at distances of 69 and 33 Mpc, and have relative velocities to their putative hosts of ~ 4300 and $\sim 1200\,{\rm km\,s^{-1}}$, respectively. Additionally, as we described above, we find no massive companions near these dwarfs. This is generally consistent with their 'possible' association classification in C21, as well as the note made by those authors regarding the challenge of deriving Sérsic models for and estimating SBF distances for dw1238−1122.

With distance estimates $D_{\rm H\,I}$ in hand, we now compute the H I mass $M_{\rm H\,I}$ using the standard relation assuming an optically thin gas (Haynes & Giovanelli 1984)

$$M_{\rm H\,I} = 2.356 \times 10^5 (D_{\rm H\,I})^2 S_{\rm H\,I}\,{\rm M_\odot}, \qquad (1)$$

where $D_{\rm H\,I}$ is in Mpc and $S_{\rm H\,I}$ is the H I flux in Jy km s^{-1} computed by integrating over the H I profile. We estimate the uncertainty on the H I mass following the methods of Springob et al. (2005) and including the 5 Mpc distance uncertainty in quadrature. We determine dw0934+2204 and dw1238−1122 have $\log(M_{\rm H\,I}/{\rm M_\odot}) = 8.29$ and 8.17, respectively, which are comparable to some of the gas-rich Local Volume dwarfs (see Fig. 5) and the broader gas-rich dwarf population (Huang et al. 2012; Poulain et al. 2022). We list these derived properties and their uncertainties in Table 2. As part of our aforementioned search for interlopers, we found no massive systems that could be possible hosts for these two background systems and consider them to be dwarf galaxies in the field.

4.1.1 GALEX *UV Photometry of new H I detections*

We perform aperture photometry of deep[6] archival *GALEX* UV imaging for the two detections in our sample to complement their H I derived properties. We follow the curve-of-growth method described in Karunakaran et al. (2021) to find the optimal radius at which fluxes are measured. To estimate the background and noise, we place 1000 equal-sized background apertures in 15 × 15 arcmin^2 cutout images centred on the dwarf and take the mean as the background value and the standard deviation as the noise. We compute AB apparent magnitudes using the standard equations (Morrissey et al. 2007) (see Table 3) and correct for foreground extinction using $E(B-V)$ from Schlafly & Finkbeiner (2011) with $R_{\rm NUV} = 8.2$ and $R_{\rm FUV} = 8.24$ (Wyder et al. 2007). Using these extinction-corrected magnitudes and $D_{\rm HI}$ with the relations from Iglesias-Páramo et al. (2006), we estimate star formation rates (SFRs) $SFR_{\rm NUV}$ and $SFR_{\rm FUV}$. Together with these SFRs, we estimate approximate gas-consumption timescales for these field dwarf galaxies and find that, in addition to their H I properties, they are similar to the broader field dwarf galaxy population (e.g. Huang et al. 2012). We list all of these derived properties along with their *GALEX* tile names in Table 3.

4.1.2 *Optical properties of new H I detections*

We briefly discuss the optical properties of our two new H I detections. dw0934+2204 is an LSB dwarf galaxy in the field with a relatively smooth morphology, as indicated by the 'dE' classification from C20, and is blue in colour, $g - r \sim 0.3$, akin to many other LSB dwarf galaxies in low-density environments (e.g. Tanoglidis et al. 2021). On the other hand, dw1238−1122, has optical properties near the threshold criteria ($\mu_{0,g} \gtrsim 24\,{\rm mag\,arcsec^{-2}}$ and $r_{\rm eff} \gtrsim 1.5\,{\rm kpc}$) for an Ultra-Diffuse Galaxy (UDG; van Dokkum et al. 2015) with $\mu_{0,g} \sim 23.7{\rm mag\,arcsec^{-2}}$ and $r_{\rm eff} \sim 2.3$ kpc.[7] Furthermore, its relatively narrow velocity width, $W_{50,c} = 14 \pm 4\,{\rm km\,s^{-1}}$, is also consistent with the broader UDG population (e.g. Leisman et al. 2017; Karunakaran et al. 2020b; Poulain et al. 2022).

4.2 H I non-detections

For the remaining 47 sources in our sample observed with the GBT, we find no obvious H I counterparts. We place 5σ upper limits on their H I masses assuming their host distances and σ_{50} from Table 1

---

[6] i.e. exposure times > 1000 s, with the exception of a single AIS depth 100 s FUV tile

[7] C20 fit Sérsic profiles to derive effective surface brightnesses and here we have estimated $\mu_{0,\,g}$ assuming $n = 1$. Of course, $\mu_{0,\,g}$ will vary depending on the true n for this system.

Table 3. *GALEX* UV properties of dwarf satellite candidates with H I detections. Columns (2) and (3): apparent NUV and FUV magnitudes corrected for foreground extinction. Columns (4) and (5): logarithm of SFRs calculated from NUV and FUV luminosities using the relations of Iglesias-Páramo et al. (2006). Columns (6): approximate gas consumption time-scale in Gyr calculated using the FUV SFR and $M_{\mathrm{H\,I}}$ listed in Columns (9) of Table 2. Columns (7) and (8): the NUV and FUV tile names.

Name (1)	m_{NUV} (mag) (2)	m_{FUV} (mag) (3)	$\log(\frac{SFR_{\mathrm{NUV}}}{\mathrm{M_\odot\,yr^{-1}}})$ (4)	$\log(\frac{SFR_{FUV}}{\mathrm{M_\odot\,yr^{-1}}})$ (5)	T_{cons} (Gyr) (6)	NUV tile (7)	FUV tile (8)
dw0934+2204	20.9 ± 0.4	21.5 ± 0.5	-2.11 ± 0.18	-2.54 ± 0.20	~ 80	MISGCSN3_23812_0193	AIS_192_1_39
dw1238−1122	20.1 ± 0.4	20.4 ± 0.4	-2.41 ± 0.21	-2.74 ± 0.21	~ 60	NGA_NGC 4594	NGA_NGC 4594

together with a modified version of equation (1):

$$M_{\mathrm{H\,I}}^{\mathrm{lim}} = 5.89 \times 10^{7} D_{\mathrm{host}}^{2} (\sigma_{50})\,\mathrm{M_\odot}, \quad (2)$$

where we substitute the integrated flux ($S_{\mathrm{H\,I}}$) from equation (1) with $5\sigma_{50}\Delta V$ and where $\Delta V = 50\mathrm{km\,s^{-1}}$. We list $M_{\mathrm{H\,I}}^{\mathrm{lim}}$ and $M_{\mathrm{H\,I}}/L_V$ upper limits in Column 13 of Table 1. We calculate L_V using the M_V for the satellites from C21 and $M_{V,\odot} = 4.8$ (Willmer 2018). It is reasonable to assume that these satellites are at the distances of their hosts given the particular strength of the SBF distance estimation method for relatively red, early-type systems such as our non-detections (see Section 4.4.1) and, by contrast, exceptions to this trend for relatively blue, irregular systems, such as our H I detections.

Some of these sources are either confused by their host's or a nearby, more massive satellite's H I emission and we mark their names in Table 1 with a ^{b} symbol. In Fig. 2, we show the spectra of the 15 obscured targets in our observed sample. The vertical dashed lines show the approximate velocity range we expected their host H I emission to cover, i.e. their systemic velocity (short, solid vertical lines) $\pm 350\,\mathrm{km\,s^{-1}}$. From this figure, we can see that these systems have strong H I contamination from their hosts. We reiterate that we have searched through these spectra at finer spectral resolutions (i.e. down to $5\,\mathrm{km\,s^{-1}}$) than shown in Fig. 2 and still find no evidence for any potential emission associated with the satellites. We can also see that in several of these cases the entire velocity range is not contaminated as our observations have likely only partially detected the contaminating disc due to the GBT beam response pattern. That is to say, the strength and shape of the contaminating H I emission depend on the host H I disc's orientation and distance from the GBT pointing centre. These cases allow us to further constrain the velocity space that the satellite could reside in within the host's gravitational reach. So, while it is possible that a few of these sources may indeed have H I reservoirs of their own, we were unable to discern them based on the available data and higher spatial resolution H I data may provide more insight in this regard. We return to this issue in Section 4.4.

4.3 Literature H I measurements

In addition to the new GBT observations of 49 satellites, we compile H I observations for 17 satellites from the literature. We include whether or not the source has a detected H I counterpart, its integrated flux estimate, corresponding source papers, and $M_{\mathrm{H\,I}}$ or upper limit in Table 1. We estimate $M_{\mathrm{H\,I}}$ and $M_{\mathrm{H\,I}}/L_V$ assuming their host distances. 15 of these sources have confirmed H I reservoirs. We derive an upper limit for NGC 4627 because the detection listed by Wolfinger et al. (2013) is a case of confusion with its host's (NGC 4631's) H I emission. In contrast, our derived upper limit for UGC5086 stems from VLA observations with higher spatial resolution than the original detection, distinguishing the H I disc of NGC 2903 from the lack of emission at the position of UGC5086 (Irwin et al. 2009). Unsurprisingly, all of the sources from the literature are bright with $M_V \lesssim -11$ relative to the broader sample. This suggests that dedicated H I observations of fainter systems are required to push beyond what is presently available in the literature.

4.4 Comparisons of optical and H I properties

Here, we make brief comparisons of the newly derived and compiled H I properties of the satellite candidates with their optical properties to gain more insight into the interplay between various tracers. We also make general comparisons between the Local Volume sample studied here and the satellites from the Local Group.

4.4.1 *Optical colours and morphologies*

We first investigate the relationship between a satellite's optical colour, morphological class, and whether or not it has been detected in H I. In Fig. 3, we show M_V as a function of $g - r$ for satellites with H I detections or satellites with relatively stringent non-detections (i.e. $M_{\mathrm{H\,I}}/L_V \leq 2$; $\sim 1\sigma$ off the relations of Bradford et al. 2015). These systems are represented by filled symbols, whereas satellites with weaker limits on $M_{\mathrm{H\,I}}/L_V$ or were obscured by their hosts' H I emission are represented by open symbols. We separate the satellites into broad 'Late' (blue) and 'Early' (red) classes based on the morphological classifications in C20. Satellites that are detected in H I are shown as stars, while non-detections are shown as inverted triangles. We have used the $g - r$ values from C21 and we convert any $g - i$ colours listed in that work to $g - r$ using equation (1) in Carlsten et al. (2022b). We note that there are four satellites (IC239, dw0240+3903, NGC 4656, and NGC 5195) that do not have a listed $g - r$ colour in C21. For three of these sources, we convert their $B - V$ colours listed in HyperLeda (Makarov et al. 2014) to $g - r$ using the relations provided by Jester et al. (2005). For NGC 4656, we estimate $g - r$ using the SDSS photometry from Schechtman-Rook & Hess (2012). Finally, we convert these SDSS $g - r$ colours to CFHT $g - r$ using the relation derived by C20 (see their equation 2).

We focus our comparison on the satellites with H I detections and stringent non-detections, revealing an interesting and potentially insightful trend. As we move toward fainter satellites (i.e. $M_V \gtrsim -14$), they fall towards redder colours, are not detected in H I, and are predominantly early-type in their morphology. The one exception to this is dw0240+3854 ($g - r \sim 0.25$, $M_V \sim -13.5$) which is detected in H I, has a relatively blue optical colour, and through visual inspection is clearly visible in *GALEX* NUV and FUV imaging[8] despite its early-type morphology. While there are cases of host H I confusion or RFI-related issues leading to weak limits on $M_{\mathrm{H\,I}}/L_V$, we can see that the aforementioned trend is broadly true for these other systems and supports the gas-poor nature of the majority of them. We discuss this trend further in the following section.

---

[8] See Legacy Survey Viewer for a colour composite

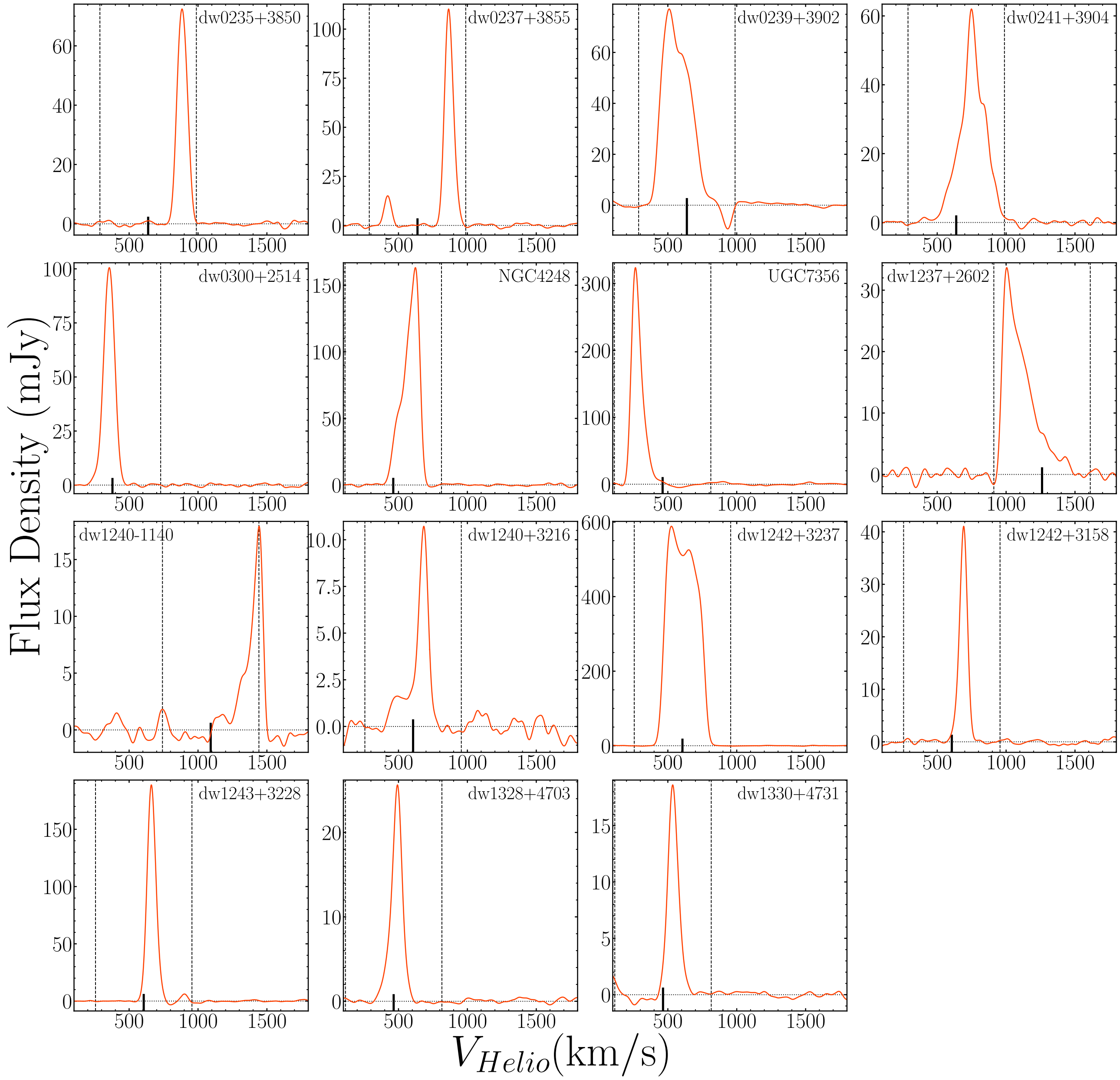

Figure 2. H I spectra for our non-detections that contain H I emission contamination from their hosts. The vertical dashed lines indicate the velocity range in which we expect the host H I emission to dominate and the short solid line shows the host systemic velocity. The horizontal dotted line shows a flux density of 0 mJy. We also indicate these affected satellites in Table 2 with a $*$ next to their names.

4.4.2 *Comparisons to the Local Group satellites*

We now turn to the Local Group and make comparisons with the sample in this work. In Fig. 4 we show Local Group (green, Putman et al. 2021) and Local Volume (orange) satellite M_V and $\log(M_{\rm H\,I}/L_V)$ as a function of separation from their hosts. We note that we exclude the NGC 1156 system from this figure as it is not in the same luminosity/mass regime as the Milky Way and M31 (C21). We show satellites with H I detections as stars and H I upper limits as inverted triangles. As in Fig. 3, we show H I detections and stringent non-detections as filled symbols, while open symbols represent satellites with host-obscured spectra or weak upper limits on $M_{\rm H\,I}/L_V$. From the top panel of Fig. 4, we can see that our H I observations are beginning to probe further down the satellite luminosity function into the region of gas-poor Local Group dwarfs. Similarly, we are beginning to probe a similar parameter space as the Local Group satellites in terms of gas-richness ($M_{\rm H\,I}/L_V$) as seen in the bottom panel of Fig. 4. However, the proximity of the bulk of the Local Group satellites leads to much more stringent limits overall. For reference, we include a horizontal dotted line indicating $M_{\rm H\,I}/L_V = 1\,{\rm M}_\odot/L_\odot$ which separates gas-poor satellites and gas-rich field dwarf galaxies. Considering both panels in Fig. 4 together suggests that we are now starting to probe a transition region between ($-10 \gtrsim M_V \gtrsim -14$) where we see a mixture of gas-rich and gas-poor satellites. We discuss this in more detail with respect to results from simulations in the following section.

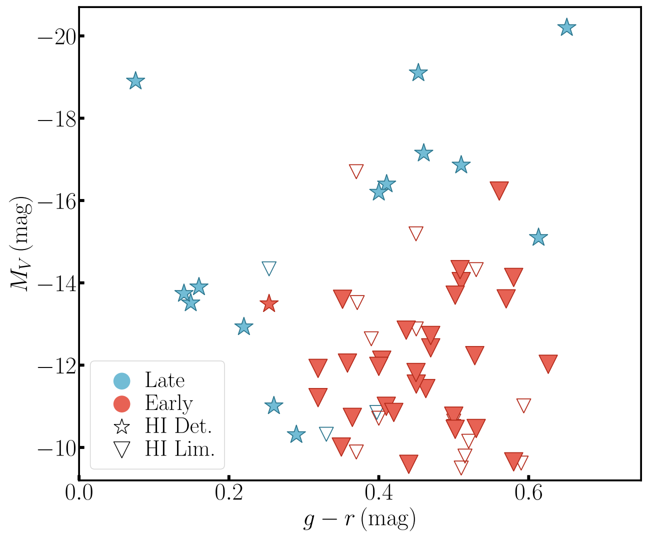

Figure 3. Comparison of M_V versus $g - r$ colour for the Local Volume sample. The symbol shapes represent H I detections (stars) and non-detections (inverted triangles), while the symbol colours correspond to the general morphological classification provided by C20, blue for late types and red for early types. We show satellites with H I detections or stringent non-detections (i.e. $M_{\rm H\,I}/L_V \leq 2$) as filled symbols, whereas satellites with weaker limits on $M_{\rm H\,I}/L_V$ or those which were obscured by their hosts' H I emission are represented by open symbols.

5 DISCUSSION AND SUMMARY

We have presented new H I observations of 49 satellites around eight Local Volume hosts using the GBT. We detect H I in two systems (dw0934+2204 and dw1238−1122) that confirm they are in the background of the Local Volume hosts near which they project. These two systems have H I and star-forming properties consistent with the field dwarf galaxy population (e.g. Huang et al. 2012) and one of which has properties near the threshold of UDGs (see Section 4.1.2).

For the remaining 47 sources in our sample, we set 5σ upper limits on their H I mass. In addition to these new observations, we compile H I measurements from the literature for 17 satellites. We compare the H I properties of these 64 satellites around Local Volume hosts to the satellites in the Local Group (see Fig. 4). We find that the gas richnesses, $M_{\rm H\,I}/L_V$, for the Local Volume satellites are broadly similar to those of the Local Group. Furthermore, with this sample of satellites that push to even fainter optical luminosities, we are beginning to probe a transition region between $-10 \gtrsim M_V \gtrsim -14$. Dwarf satellites above this threshold are predominantly star-forming and gas-rich, while those below it are quenched and gas poor. This trend is more clearly seen in Fig. 3 where we show only the Local Volume sample and distinguish satellites by their optical morphology and whether or not they were detected in H I. While we are beginning to probe this transition region, we note that the complete transition from gas-rich to gas-poor can only be seen in the Local Group since it reaches well into the fully-quenched, ultrafaint dwarf regime. Nevertheless, seeing the beginning of this transition region is an interesting and insightful consistency that we also see in the Local Group (Fig. 4; Putman et al. 2021) and is the first observational demonstration of such a trend around other Milky Way-like systems. While many of the satellites in this transition region are gas-poor, some are gas-rich. This result suggests that the transition between predominantly gas-poor and gas-rich satellites occurs at $L_V \sim 10^7 L_\odot$, in line with predictions from simulations (Fillingham et al. 2015; Simpson et al. 2018; Akins et al. 2021; Samuel et al. 2022). Furthermore, this consistency suggests that similar quenching processes typically invoked for dwarf galaxies in the Local Group are likely to be at play in these other systems. Similarly, more massive satellites have been shown to be quenched and/or gas-poor in accordingly higher density environments such as groups and clusters (Brown et al. 2015, 2017; Jones et al. 2020), reaffirming the greater susceptibility of lower mass haloes to environmental effects leading to their eventual quenching as seen in hydrodynamical simulations (Fillingham et al. 2016; Garrison-Kimmel et al. 2019; Samuel et al. 2022). Compiling existing and obtaining new H I observations would allow for quantitative comparisons to theoretical predictions beyond the qualitative initial comparisons discussed here.

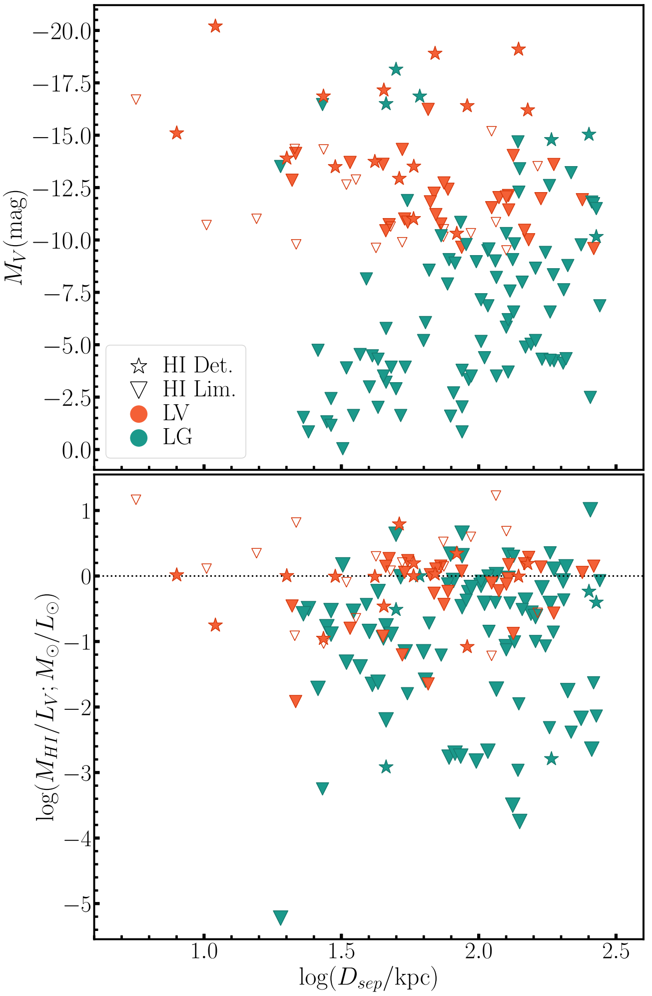

Figure 4. Comparisons of the V-band absolute magnitudes (top panel) and H I mass to V-band luminosity ratios, $M_{\rm H\,I}/L_V$, (bottom panel) as a function of separation for the Local Volume (orange symbols) and Local Group (green symbols) samples. Stars represent satellites with H I detections, while inverted triangles show those with H I mass upper limits. Filled symbols are H I detections or stringent non-detections, while open symbols are satellites with host-obscured spectra or with weak upperlimits on $M_{\rm H\,I}/L_V$. The Local Volume separations show their projected distances, whereas the Local Group separations are their true distances from either the Milky Way or M31 listed in Putman et al. (2021). The horizontal dotted line in the bottom panel indicates $M_{\rm H\,I}/L_V = 1\,{\rm M}_\odot/L_\odot$ which generally separates gas-rich field dwarfs and gas-poor satellites.

While the observations presented in this work are an important step toward understanding the H I properties of other satellite systems in the Local Volume, we briefly consider the parameter space that will

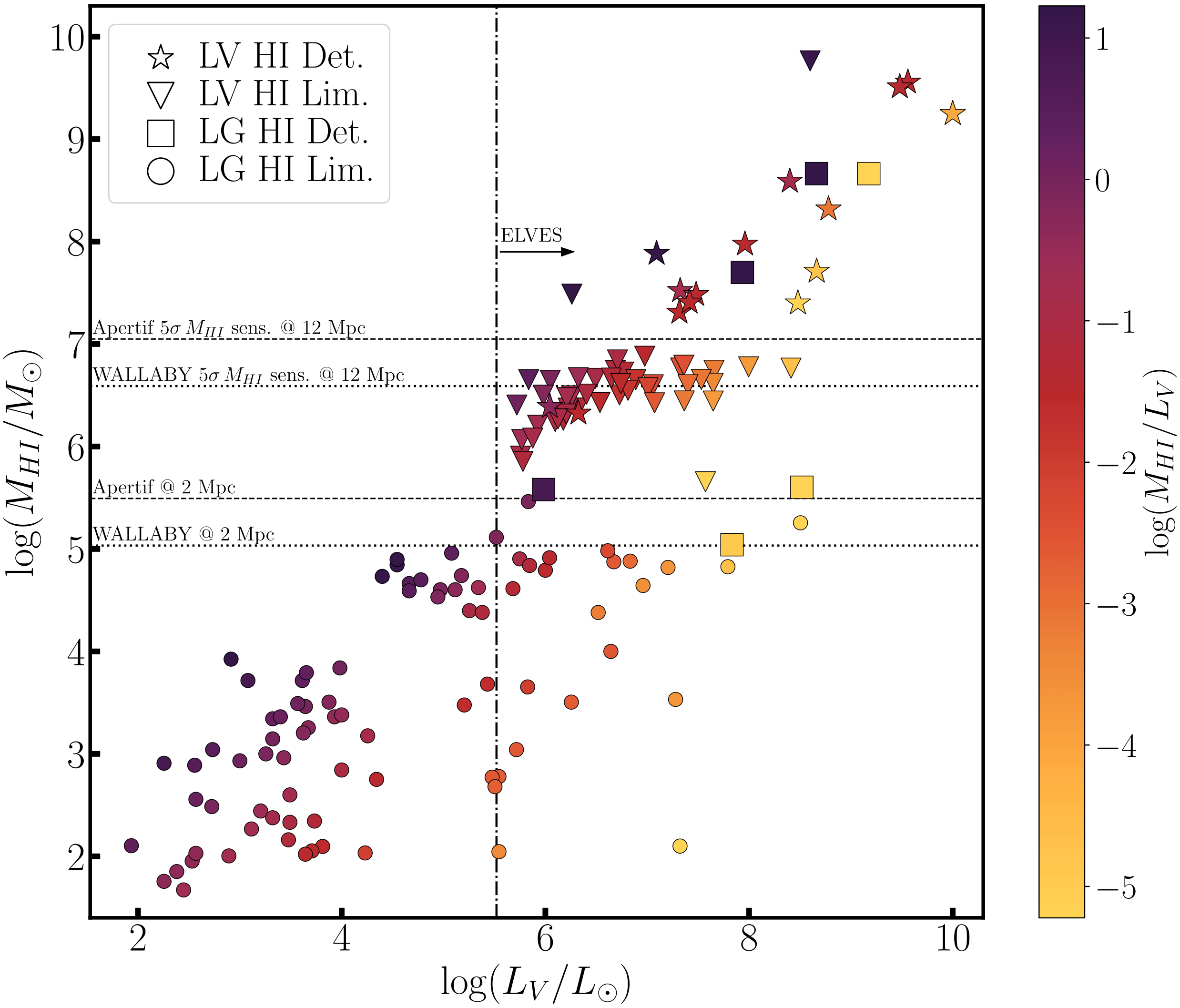

Figure 5. H I mass as a function of *V*-band luminosity for the Local Volume sample from this work (stars and inverted triangles) and the dwarf galaxies in the Local Group within 300 kpc of the Milky Way or M31 (squares and circles). The colours of the symbols show the logarithm of $M_{\mathrm{H\,I}}/L_V$. The horizontal dashed lines show the 5σ H I lower limits that are probed by the Apertif survey at distances of 2 (lower line) and 12 (upper line) Mpc. Similarly, the horizontal dotted line shows the 5σ H I lower limits probed by the WALLABY survey. It should be noted that these wide-field surveys are at much higher spatial resolutions, ∼15 and ∼30 arcsec beam widths for Apertif and WALLABY, respectively. The vertical dash–dotted line shows the completeness limit of the ELVES survey.

be probed by upcoming H I surveys. In Fig. 5, we show log($M_{\mathrm{H\,I}}$) as a function of log(L_V) for the Local Volume (stars and triangles) and Local Group (squares and circles) satellites coloured by their gas richness, log($M_{\mathrm{H\,I}}/L_V$). The horizontal dashed lines and dotted lines show the estimated minimum $M_{\mathrm{H\,I}}$ that will be probed by the upcoming Apertif survey data releases (van Cappellen et al. 2022; Hess et al. in preparation) and upcoming WALLABY (Koribalski et al. 2020) survey, respectively, at distances of 2 Mpc (lower lines) and 12 Mpc (upper lines). Furthermore, we note that these estimates assume unresolved 5σ sources with velocity widths of 50 km s^{-1}. The aforementioned transition region can be seen ($L_V \sim 10^6$–$10^{7.5} L_\odot$) with a mix of H I detections (stars and squares) and non-detections (triangles and circles). While we are able to reach similar satellite gas richness limits with the deep observations presented in this work to those in the Local Group, confirming this transition region requires a larger sample of satellites and H I observations.

More quantitative comparisons may be made using the Exploration of Local VolumE Satellites (ELVES) Survey (Carlsten et al. 2022a). The ELVES sample extends the one used in this work and consists of over 300 confirmed satellites around 30 Local Volume hosts with more uniform spatial coverage within 300 kpc and similar photometric completeness, vertical dashed-dotted line in Fig. 5. This sample will populate the aforementioned transition region and with additional H I constraints, we can place statistically significant constraints on this region. Furthermore, the additional spatial coverage will enable studies of gas-richness as a function of radial separation. The Apertif and WALLABY survey areas include 8 and 18 of the ELVES systems, respectively. Of these 24 systems with Apertif and WALLABY coverage, eight were studied in this work albeit with significantly less spatial completeness. So, while we were able to identify some potentially interesting trends, such as the one between colour, morphology, and H I emission from

Fig. 3, the increased sample size will solidify their validity. These H I surveys will not only provide great sensitivity but their spatial resolution (Apertif ∼ 15 arcsec, WALLABY ∼ 30 arcsec) will reduce the occurrence of host H I confusion, may resolve the H I distributions in the most massive satellites, and possibly detect the remnants of past interactions (i.e. H I streams).

There is still much to be done until these upcoming surveys are fully on-line and/or their data analysed. With this in mind, we have initiated additional follow-up surveys to characterize the H I and star-forming properties of satellite galaxies in the Local Universe. This initial follow-up effort aims to set the groundwork for what future wide-field H I surveys, like WALLABY, will tell us.

ACKNOWLEDGEMENTS

We thank the referee for their useful comments that helped improve the quality of this work. We thank Kelley M. Hess for useful discussions regarding the Apertif survey. AK acknowledges financial support from the State Agency for Research of the Spanish Ministry of Science, Innovation and Universities through the 'Center of Excellence Severo Ochoa' awarded to the Instituto de Astrofísica de Andalucía (SEV-2017-0709), from grant RTI2018-096228-B-C31 (MCIU/AEI/FEDER,UE) and through the grant POSTDOC_21_00845 financed from the budgetary program 54a Scientific Research and Innovation of the Economic Transformation, Industry, Knowledge and Universities Council of the Regional Government of Andalusia. KS acknowledges support from the Natural Sciences and Engineering Research Council of Canada (NSERC). BMP is supported by an NSF Astronomy and Astrophysics Postdoctoral Fellowship under award AST2001663. Research by DC is supported by NSF grant AST-1814208. DJS acknowledges support from NSF grants AST-1821967 and 1813708.

DATA AVAILABILITY

The raw and reduced H I spectra from the GBT used in this work as well as the derived properties listed in Tables 1–3 may be shared upon request to A. Karunakaran.

REFERENCES

Akins H. B., Christensen C. R., Brooks A. M., Munshi F., Applebaum E., Engelhardt A., Chamberland L., 2021, ApJ, 909, 139
Bennet P., Sand D. J., Crnojević D., Spekkens K., Zaritsky D., Karunakaran A., 2017, ApJ, 850, 109
Bennet P., Sand D. J., Crnojević D., Spekkens K., Karunakaran A., Zaritsky D., Mutlu-Pakdil B., 2019, ApJ, 885, 153
Bennet P., Sand D. J., Crnojević D., Spekkens K., Karunakaran A., Zaritsky D., Mutlu-Pakdil B., 2020, ApJ, 893, L9
Bradford J. D., Geha M. C., Blanton M. R., 2015, ApJ, 809, 146
Braun R., Thilker D., Walterbos R. A. M., 2003, A&A, 406, 829
Brown T., Catinella B., Cortese L., Kilborn V., Haynes M. P., Giovanelli R., 2015, MNRAS, 452, 2479
Brown T. et al., 2017, MNRAS, 466, 1275
Bullock J. S., Boylan-Kolchin M., 2017, ARA&A, 55, 343
Carlin J. L. et al., 2016, ApJ, 828, L5
Carlsten S. G., Beaton R. L., Greco J. P., Greene J. E., 2019, ApJ, 878, L16
Carlsten S. G., Greco J. P., Beaton R. L., Greene J. E., 2020, ApJ, 891, 144 (C20)
Carlsten S. G., Greene J. E., Greco J. P., Beaton R. L., Kado-Fong E., 2021, ApJ, 922, 267 (C21)
Carlsten S. G., Greene J. E., Beaton R. L., Danieli S., Greco J. P., 2022a, ApJ, 933, 47
Carlsten S. G., Greene J. E., Beaton R. L., Greco J. P., 2022b, ApJ, 927, 44
Chiboucas K., Karachentsev I. D., Tully R. B., 2009, AJ, 137, 3009
Chiboucas K., Jacobs B. A., Tully R. B., Karachentsev I. D., 2013, AJ, 146, 126
Courtois H. M., Tully R. B., 2015, MNRAS, 447, 1531
Crnojević D. et al., 2016, ApJ, 823, 19
Crnojević D. et al., 2019, ApJ, 872, 80
Dahlem M., Ehle M., Ryder S. D., Vlajić M., Haynes R. F., 2005, A&A, 432, 475
Fattahi A. et al., 2016, MNRAS, 457, 844
Fillingham S. P., Cooper M. C., Wheeler C., Garrison-Kimmel S., Boylan-Kolchin M., Bullock J. S., 2015, MNRAS, 454, 2039
Fillingham S. P., Cooper M. C., Pace A. B., Boylan-Kolchin M., Bullock J. S., Garrison-Kimmel S., Wheeler C., 2016, MNRAS, 463, 1916
Font A. S., McCarthy I. G., Belokurov V., Brown S. T., Stafford S. G., 2022, MNRAS, 511, 1544
Garrison-Kimmel S. et al., 2019, MNRAS, 489, 4574
Geha M., Blanton M. R., Yan R., Tinker J. L., 2012, ApJ, 757, 85
Geha M. et al., 2017, ApJ, 847, 4
Grcevich J., Putman M. E., 2009, ApJ, 696, 385
Haynes M. P., Giovanelli R., 1984, AJ, 89, 758
Haynes M. P. et al., 2018, ApJ, 861, 49
Huang S., Haynes M. P., Giovanelli R., Brinchmann J., Stierwalt S., Neff S. G., 2012, AJ, 143, 133
Iglesias-Páramo J. et al., 2006, ApJS, 164, 38
Irwin J. A. et al., 2009, ApJ, 692, 1447
Javanmardi B. et al., 2016, A&A, 588, A89
Jester S. et al., 2005, AJ, 130, 873
Jones M. G., Hess K. M., Adams E. A. K., Verdes-Montenegro L., 2020, MNRAS, 494, 2090
Karachentsev I. D. et al., 2015, Astrophys. Bull., 70, 379
Karunakaran A., Spekkens K., Bennet P., Sand D. J., Crnojević D., Zaritsky D., 2020a, AJ, 159, 37
Karunakaran A., Spekkens K., Zaritsky D., Donnerstein R. L., Kadowaki J., Dey A., 2020b, ApJ, 902, 39
Karunakaran A. et al., 2021, ApJ, 916, L19
Koribalski B. S. et al., 2020, Ap&SS, 365, 118
Leisman L. et al., 2017, ApJ, 842, 133
Makarov D., Prugniel P., Terekhova N., Courtois H., Vauglin I., 2014, A&A, 570, A13
Mao Y.-Y., Geha M., Wechsler R. H., Weiner B., Tollerud E. J., Nadler E. O., Kallivayalil N., 2021, ApJ, 907, 85
Merritt A., van Dokkum P., Abraham R., 2014, ApJ, 787, L37
Morrissey P. et al., 2007, ApJS, 173, 682
Müller O., Scalera R., Binggeli B., Jerjen H., 2017, A&A, 602, A119
Mutlu-Pakdil B. et al., 2021, ApJ, 918, 88
Mutlu-Pakdil B. et al., 2022, ApJ, 926, 77
Poulain M. et al., 2022, A&A, 659, A14
Putman M. E., Zheng Y., Price-Whelan A. M., Grcevich J., Johnson A. C., Tollerud E., Peek J. E. G., 2021, ApJ, 913, 53
Samuel J., Wetzel A., Santistevan I., Tollerud E., Moreno J., Boylan-Kolchin M., Bailin J., Pardasani B., 2022, MNRAS, 514, 5276
Sancisi R., van Woerden H., Davies R. D., Hart L., 1984, MNRAS, 210, 497
Sand D. J. et al., 2022, ApJ, 935, L17
Schechtman-Rook A., Hess K. M., 2012, ApJ, 750, 171
Schlafly E. F., Finkbeiner D. P., 2011, ApJ, 737, 103
Simpson C. M., Grand R. J. J., Gómez F. A., Marinacci F., Pakmor R., Springel V., Campbell D. J. R., Frenk C. S., 2018, MNRAS, 478, 548
Smercina A., Bell E. F., Price P. A., D'Souza R., Slater C. T., Bailin J., Monachesi A., Nidever D., 2018, ApJ, 863, 152
Spekkens K., Mason B. S., Aguirre J. E., Nhan B., 2013, ApJ, 773, 61
Spekkens K., Urbancic N., Mason B. S., Willman B., Aguirre J. E., 2014, ApJ, 795, L5
Springob C. M., Haynes M. P., Giovanelli R., Kent B. R., 2005, ApJS, 160, 149
Tanoglidis D. et al., 2021, ApJS, 252, 18
Teyssier M., Johnston K. V., Kuhlen M., 2012, MNRAS, 426, 1808
van Albada G. D., 1977, A&A, 61, 297
van Cappellen W. A. et al., 2022, A&A, 658, A146

van Dokkum P. G., Abraham R., Merritt A., Zhang J., Geha M., Conroy C., 2015, ApJ, 798, L45

Wetzel A. R., Hopkins P. F., Kim J.-h., Faucher-Giguère C.-A., Kereš D., Quataert E., 2016, ApJ, 827, L23

Willmer C. N. A., 2018, ApJS, 236, 47

Wolfinger K., Kilborn V. A., Koribalski B. S., Minchin R. F., Boyce P. J., Disney M. J., Lang R. H., Jordan C. A., 2013, MNRAS, 428, 1790

Wyder T. K. et al., 2007, ApJS, 173, 293

Zaritsky D., Smith R., Frenk C., White S. D. M., 1993, ApJ, 405, 464

Zaritsky D., Smith R., Frenk C., White S. D. M., 1997, ApJ, 478, 39

This paper has been typeset from a TEX/LATEX file prepared by the author.